Energy Conversion and Management 243 (2021) 114414

Contents lists available at ScienceDirect

Energy Conversion and Management

journal homepage: www.elsevier.com/locate/enconman

Exploring the potential benefits of using metasurface for galloping energy harvesting

Junlei Wang [a], Shaokang Sun [a], Guobiao Hu [b,*], Yaowen Yang [b], Lihua Tang [c], Pan Li [a,*], Guojie Zhang [a]

[a] School of Mechanical and Power Engineering, Zhengzhou University, Zhengzhou 450000, China
[b] School of Civil and Environmental Engineering, Nanyang Technological University, 50 Nanyang Avenue, 639798, Singapore
[c] Department of Mechanical Engineering, The University of Auckland, Auckland, New Zealand

ARTICLE INFO

Keywords:
Metasurface
Galloping
Three-dimensional CFD simulation
Piezoelectric energy harvesting

ABSTRACT

Inspired by the successful applications of metasurfaces in many other fields, this paper aims to explore the potential application of metasurfaces in designing aerodynamic systems. Bluff bodies are proposed to be wrapped in metasurfaces for improving galloping energy harvesting. Three different metasurfaces with convex cylinder, tri-prim, and wedge ornaments are designed. A general aeroelastic model for a galloping energy harvester is developed. The aerodynamic force is represented by a polynomial function with its coefficients being determined from three-dimensional CFD simulations. Subsequently, physical prototypes of the proposed galloping piezoelectric energy harvesters are fabricated, and experimental tests are conducted. The theoretical model is validated by the experimental results. The analytical method and three-dimensional CFD simulation are combined to predict the dynamic responses of the metasurface-wrapped GPEHs. Besides, the results show that the metasurface can significantly change the aerodynamic characteristics of the bluff body, and it is learned that a bluff body wrapped in convex cylinder metasurface could bring benefits for promoting galloping energy harvesting performance. Further experimental studies are conducted to reveal the effects of convex ornament parameters on the galloping energy harvesting performance. It is found that using the metasurface distributed with convex cylinder ornaments of diameter 6 mm and height 9 mm leads to the largest vibration displacement and largest voltage output. Compared to the typical GPEH, the maximum vibration displacement and maximum output voltage of the proposed galloping piezoelectric energy harvester can be increased by 26.81% and 26.14%, respectively. The vortex shedding processes around the wind flow fields near the bluff bodies wrapped in metasurfaces are simulated. The underlying aerodynamic mechanism of the influence of the metasurfaces is unveiled. Finally, based on the validated theoretical model, a parametric study is carried out to investigate the effects of the load resistance and electromechanical coupling strength on the galloping energy harvesting performance. It is concluded that increasing the coupling strength to a certain level and tuning the load resistance to the optimal value could further improve the power output. However, when the electromechanical coupling strength increases to a certain extent, the power output will reach the saturation state, and the coupling strength is extremely large. Therefore, a piezoelectric element with a moderate coupling coefficient is recommended for practical applications from the perspective of economic benefit.

1. Introduction

In the past few decades, due to the massive consumption of non-renewable fossil fuels, the energy crisis problem is becoming more serious, accompanied by severe environmental degradation. Many researchers are devoted to developing clean power generation technologies to address the above issues by collecting renewable energy from nature, such as solar energy, water energy, heat energy, wind energy, etc. Wind farms are typical products of such kinds of technologies. With the advance of microelectronic technology, the power consumption of electronic devices has been significantly reduced by several orders of magnitude. The above concept has been extended to small-scale energy generation in recent years for replacing chemical batteries to power micro-electro-mechanical-systems (MEMS) and wireless sensor

---

* Corresponding authors.
E-mail addresses: guobiao.hu@ntu.edu.sg (G. Hu), lipan@zzu.edu.cn (P. Li).

https://doi.org/10.1016/j.enconman.2021.114414
Received 15 March 2021; Accepted 11 June 2021

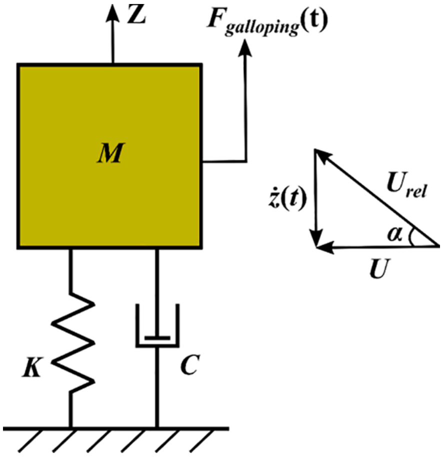

Fig. 1. Schematic diagram of a bluff body that undergoes galloping.

networks (WSNs) [1–12].

As a ubiquitous resource in the environment, the wind is one of the most important renewable energy sources that humans can efficiently harness for the current. Traditional wind-induced vibration needs to be suppressed to avoid structural failure and damage. Studies have been conducted by some researchers, e.g., Chen et al. [13] comprehensively investigated the vortex induced vibration of a flexible cable under a shear flow in experiments. On the other hand, to convert wind energy into electrical energy using a relatively compact structure, rather than rotary machinery, systems are often designed to harvest the energy from flow-induced vibrations as the consequence of fluid–structure interaction (FSI). These kinds of devices are termed flow-induced vibration energy harvesters (FIVEHs). The vibration-to-electricity conversion can be realized through various transduction mechanisms, such as electromagnetic [14,15], triboelectric [16–18], piezoelectric [19–22], and electrostatic effects [23–25]. A lot of wind energy harvesters adopted piezoelectric transducers for energy transduction since they are easy to implement and of high power density [26].

Galloping is a typical self-excited oscillation phenomenon caused by aeroelastic instability [27]. Unlike other types of FIVs (vortex-induced vibration [13,28–30], flutter, buffeting, etc.), galloping can be initiated under a low wind speed and result in a high-amplitude oscillation. Moreover, increasing the wind speed can monotonically boost the high-amplitude oscillation [31]. Therefore, galloping piezoelectric energy harvesters (GPEHs) have been widely regarded as suitable candidates for harvesting wind energy. To improve the performance of GPEHs, some researchers have proposed techniques for introducing nonlinear forces. Alhadidi et al. [32] proposed a galloping-based piezoelectric energy harvester (GPEH) with magnetic forces. They discussed the effects of different magnetic forces on the performance of the GPEH. Dai et al. [33] established a nonlinear distributed parameter model and compared the performance of the GPEHs with different aerodynamic characteristics. From the electrical perspective, some researchers attempted to optimize the shunt circuits to facilitate galloping vibration. Tan et al. [34] provided a simplified optimization method of an inductive-resistive circuit for broadband piezoelectric energy harvester, and introduced series and parallel inductor-resistor circuits. Zhao et al. [35] pointed out that the interface circuits are also very important in affecting the performance of GPEHs. The application of synchronous charge extraction circuit (SCE), standard circuit, series, and parallel synchronous switching inductor circuits (SSHI) in galloping energy harvesting were analyzed. In addition, others attempted to modify the geometric profile of the bluff body to change the aerodynamic characteristics for promoting galloping oscillation. Through experiments, Yang et al. [36] compared the performance of wind energy harvesters with different cross-section shapes (square, rectangle, triangle, and D-shape). The results indicated that the square cross-section led to a lower threshold wind speed and higher power output. Based on the traditional bluff body with a square cross-section, Wang et al. [37] devised the novel spindle-like and butterfly-like bluff bodies, which coupled vortex-induced vibration (VIV) and galloping phenomena. The results showed that the minimum width ratio of the vertical spindle-like bluff body could reduce the threshold wind speed by more than 13% and increase the maximum output voltage by more than 160% compared to the conventional GPEH. Besides, Hu et al. [38] investigated the performance of a galloping energy harvester with fins installed in different positions of the square prism by wind tunnel experiments. Noel et al. [39] added a rigid splitter plate at the end of the prism column to consider its effect on the flow field around the prism column. It was proven that the effective range of aerodynamic instability could be expanded in this way, and a larger oscillation amplitude and power output could be obtained. Zhu et al. [40] introduced an attached free-to-rotate pentagram impeller device on a circular cylinder. Based on the CFD simulation, they found that the rotation of the pentagram impeller would have a strong interference on the trailing vortices falling behind the cylinder, transforming the oscillation of the bluff body from vortex-induced vibration to galloping with the increase of flow velocity. Similarly, for a VIV-based PEH proposed in [41], such a VIV-to-galloping transition phenomenon was also observed due to the introduction of Y-shaped appendages.

In recent years, metasurfaces with unique properties have been extensively applied in various disciplines, e.g., electromagnetics [42,43], thermology [44,45], and acoustics [46,47]. Amer et al. [48] constructed an electromagnetic energy acquisition system based on a wide-angle metasurface to capture electromagnetic waves efficiently. Wang et al. [49] reviewed the latest research of thermal metamaterials and showed that metasurfaces are widely used in various thermal functional devices. Liu et al. [50] proposed an acoustic metasurface with sub-wavelength thickness for potential application in underwater acoustic communication and medical ultrasound imaging. Though numerous successful applications of metasurfaces have been reported in many other fields, utilizing metasurfaces to design systems for galloping-based energy harvesting has not been found in the field of aerodynamics. Inspired by the modified bluff bodies with attachments, this paper explores the idea of wrapping ordinary cuboid bluff bodies in three metasurfaces with different ornaments, namely, convex cylinder, convex triprism, and convex wedge. Since the aerodynamic behaviors of the bluff bodies are altered due to the introduction of the metasurfaces, the three-dimensional CFD simulation is used to determine the aerodynamic force coefficients of the modified bluff bodies.

The rest of this paper is organized as follows. In Section 2, the theoretical model of a galloping-based piezoelectric energy harvester (GPEH) is established. Based on the quasi-steady-state theory, the analytical method and three-dimensional CFD simulation are combined to predict the dynamic responses of the metasurface-wrapped GPEHs, which are termed as Meta-GPEHs for short hereinafter. Section 3 presents the designed prototypes and experimental setup. The established theoretical model is validated by wind tunnel experiments in Section 4. Moreover, by varying the convex cylinder ornament height, the experimental results of the bluff bodies wrapped in the metasurfaces are discussed. In Section 5, the vortex shedding processes of different bluff bodies in Section 4 are simulated by CFD to explain the underlying mechanisms. Besides, based on the theoretical model, parametric analyses are carried out to investigate the influences of the electrical load resistance and the electromechanical coupling strength on the energy harvesting performance. Finally, relevant conclusions are summarized in Section 6.

2. Modeling

2.1. Theoretical model

Fig. 1 shows the diagram of a bluff body that undergoes galloping.

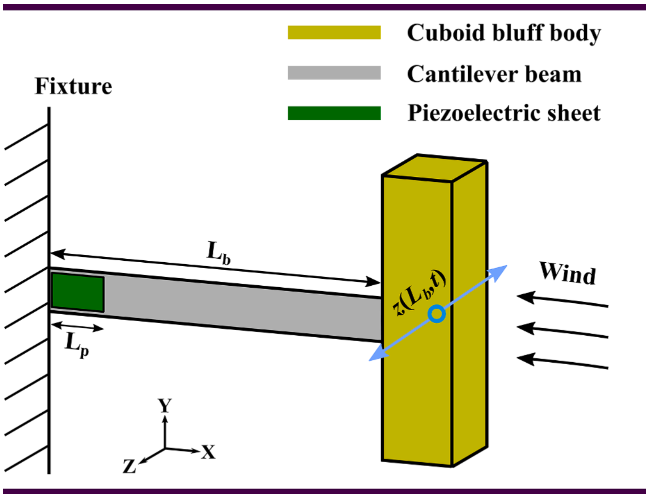

Fig. 2. Schematic diagram of a typical GPEH.

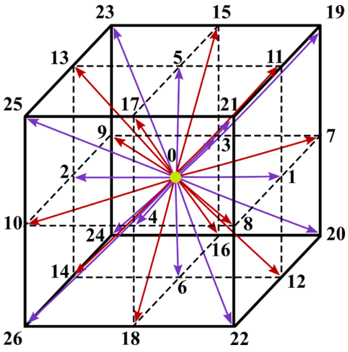

Fig. 3. D3Q27 discrete velocity model.

Table 1
Parameter values of the incoming flow ($T = 288.15$ K).

Description	Symbols	Values/Units
Thermal conductivity	λ	0.0243 W·(m·K)$^{-1}$
Reference density	ρ	1.2041 kg·m^{-3}
Dynamic viscosity	ν	1.7894e-5 Pa·s
Molecular weight	M_{ol}	28.996 g /mol
Specific heat capacity	c	1006.43 J·(kg·K)$^{-1}$

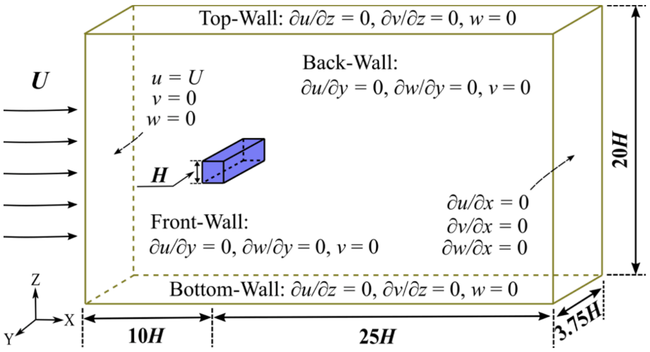

Fig. 4. Schematic of the computation domain and boundary conditions.

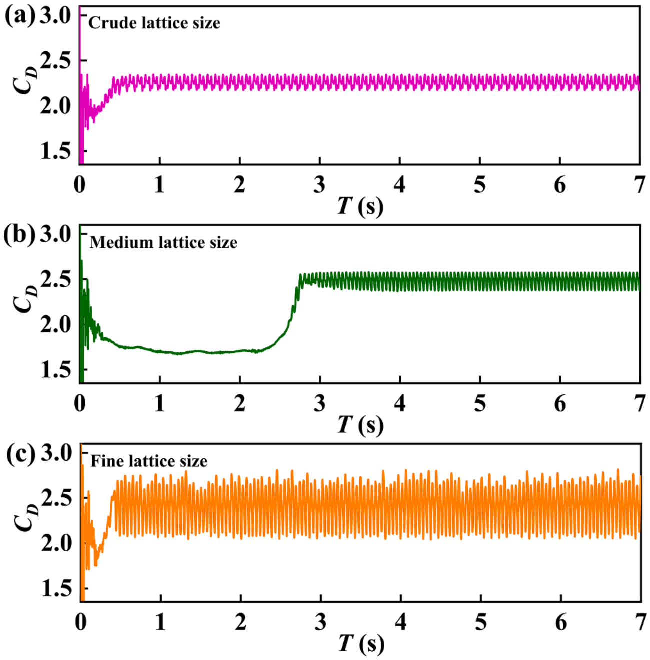

Fig. 5. The time history responses of the drag coefficient for (a) crude lattice size; (b) medium lattice size; (c) fine lattice size.

Table 2
Comparison of the lift and drag coefficients computed using different lattice sizes.

Size	Lattice numbers	C_{Lrms}	C_D
Crude	890,600	1.197	2.255
Medium	1,516,800	1.467	2.483
Fine	3,448,960	1.443	2.431

The elastically mounted bluff body oscillates in the z-direction under the aerodynamic force produced by a uniform wind flow of a constant speed U. The governing equation of the galloping bluff body can be written as:

$$M\ddot{z}(t) + C\dot{z}(t) + Kz(t) = F_{galloping}(t) \tag{1}$$

where M is the mass of the bluff body; C is the system damping; K is the spring stiffness; and $z(t)$ is the translational displacement of the bluff body. The aerodynamic force in Eq. (1) can be expressed as:

$$F_{galloping}(t) = 0.5\rho S_c U^2 C_{Fz} \tag{2}$$

where ρ is the air density;$S_c = H \times L_0$ is the cross-sectional area (normal to the wind flow), where H is the characteristic length of the bluff body and L_0 is the length of the bluff body.C_{Fz} is the coefficient of the vertical component of the fluid-dynamic force, which can be expressed by a polynomial function as:

$$C_{Fz} = \sum_{i=1}^{n} A_i(\alpha)^i \tag{3}$$

where A_i ($i = 1,2, \ldots$, n) are the coefficients for the polynomial fitting function. They can be determined using the least square method based on the data obtained from wind tunnel experiments or CFD simulations. The angle of attack α is:

$$\alpha = \arctan\frac{\dot{z}(t)}{U} \tag{4}$$

When $\dot{z}(t)$ is small, Eq. (4) can be approximated as:

$$\alpha = \frac{\dot{z}(t)}{U} \tag{5}$$

Substituting Eq. (2) into Eq. (1), the governing equation can be rearranged as:

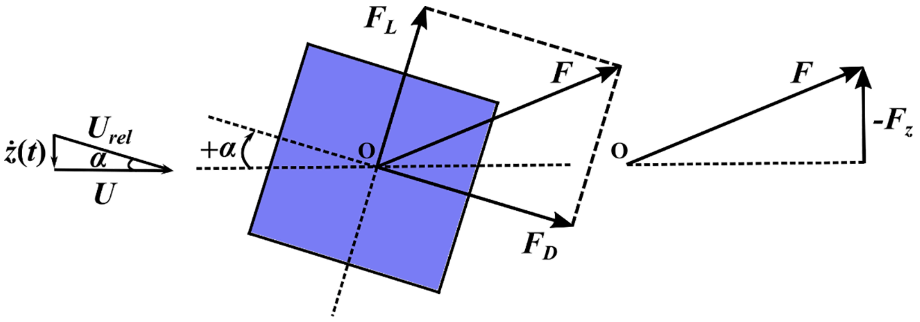

Fig. 6. Definition of angle of attack and aerodynamic forces.

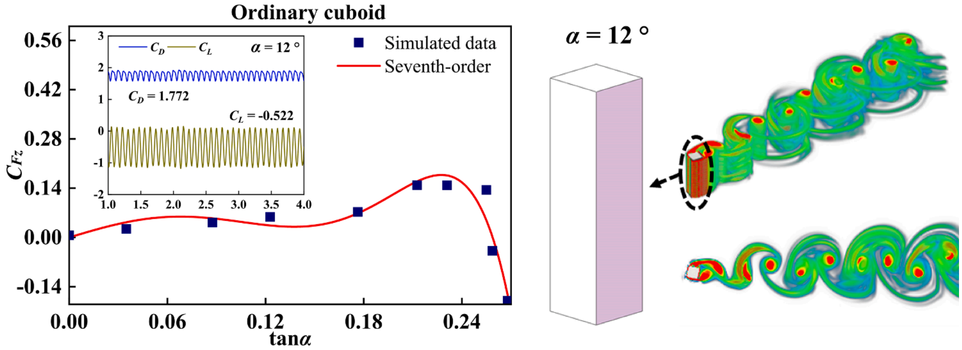

Fig. 7. Aerodynamic force coefficient C_{Fz} for the ordinary cuboid bluff body.

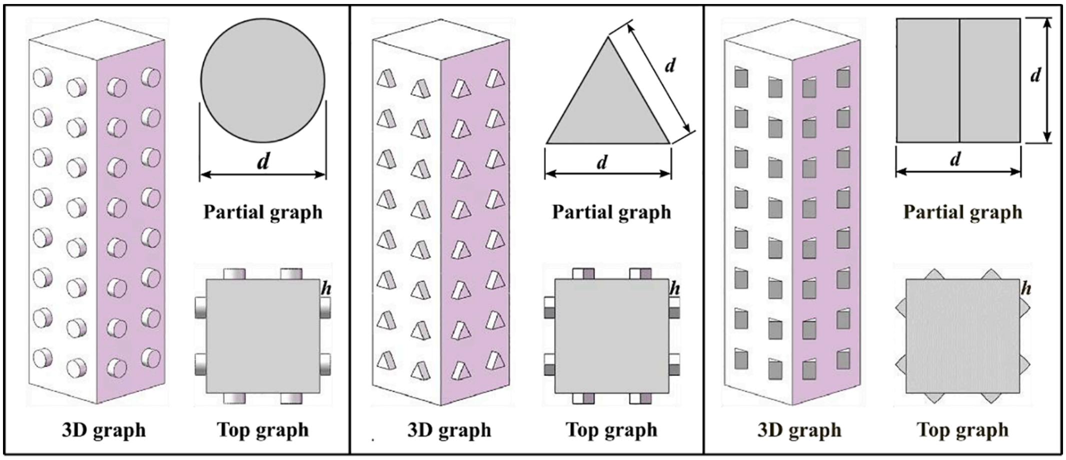

(a) Convex C-*d*6*h*3 **(b) Convex T-*d*6*h*3** **(c) Convex W-*d*6*h*3**

Fig. 8. The bluff bodies wrapped in metasurfaces with different ornaments: (a) Convex C-*d*6*h*3; (b) Convex T-*d*6*h*3; (c) Convex W-*d*6*h*3.

$$M\ddot{z}(t)+\left\{C-0.5\rho S_c U\left[\sum\nolimits_{i=1}^{n}A_i\left(\frac{\dot{z}(t)}{U}\right)^{i-1}\right]\right\}\dot{z}(t)+Kz(t)=0 \tag{6}$$

From the mathematical form of Eq. (6), the aerodynamic force can be regarded as an effective damping term. The linear and nonlinear components of the overall damping are separately written as:

$$linear\ \ C-0.5\rho S_c U A_1 \tag{7a}$$

$$nonlinear\ \ -0.5\rho S_c U\left[\sum\nolimits_{i=2}^{n}A_i\left(\frac{\dot{z}(t)}{U}\right)^{i-1}\right] \tag{7b}$$

According to Eqs. (6), (7a), and (7b), when the wind speed U is small, the system is dominated by the positive linear damping term. In other words, any small disturbance will be eventually damped out, and the system will stabilize at the equilibrium position. If U gradually increases to a critical value, i.e., $U_{cr} = 2C/(\rho S_c A_1)$, the total linear damping component becomes negative. As a consequence, the system loses stability and starts to vibrate until reaching a steady state. It is thus known that the linear damping term determines the cut-in wind speed. However, as the system starts to vibrate, the higher-order nonlinear term plays the role of a resistance to prevent the vibration amplitude from unboundedly increasing. In other words, the higher-order nonlinear damping term restricts the oscillation amplitude of the galloping system.

The schematic diagram of a typical galloping-based piezoelectric energy harvester (GPEH) is shown in Fig. 2. A piezoelectric sheet (PZT-5, $L_p \times W_p \times T_p = 30$ mm × 20 mm × 0.5 mm) is bonded at the clamped end of the elastic cantilever beam ($L_b \times W_b \times T_b = 143$ mm × 25 mm × 0.5 mm). The other end of the cantilever beam is attached with a cuboid

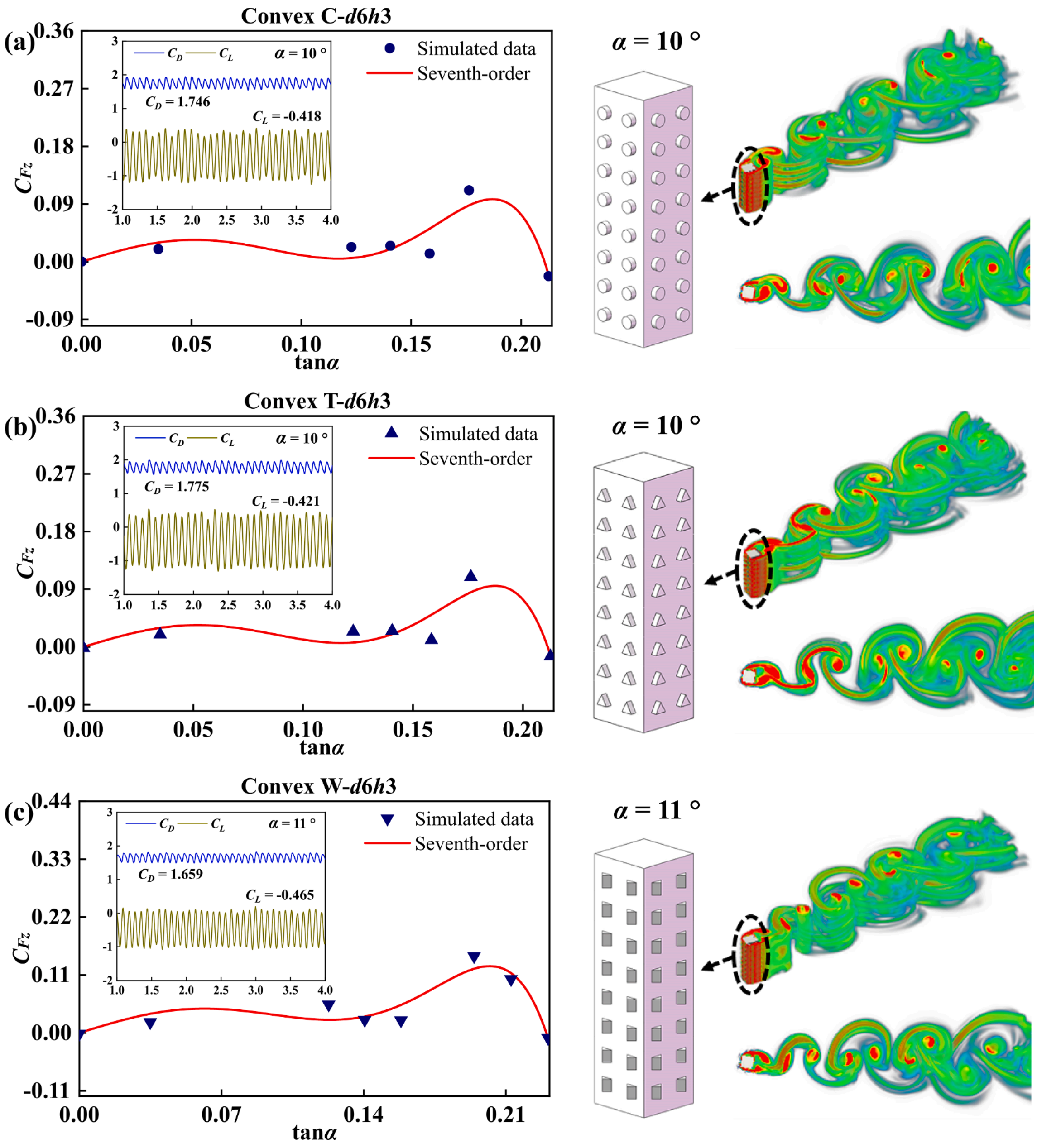

Fig. 9. Aerodynamic force coefficients C_{Fz} for bluff bodies wrapped in metasurfaces with different ornaments: (a) Convex C-*d*6*h*3; (b) Convex T-*d*6*h*3; (c) Convex W-*d*6*h*3.

Table 3
Fitting coefficients of C_{Fz} for bluff bodies wrapped in different metasurfaces.

Bluff body surface	A_1	A_3	A_5	A_7
Smooth surface	2.11	−100.31	4000	−57900
Convex C-*d*6*h*3	1.97	−63.81	4000	−63000
Convex T-*d*6*h*3	1.97	−71.81	4000	−57900
Convex W-*d*6*h*3	1.88	−67.31	4000	−57900

bluff body. The length and the height of the cuboid bluff body are, respectively, $L_0 = 120$ mm and $H = 32$ mm. Though distributed parameter models have been developed in previous studies in the existing literature [51], when an energy harvester undergoes galloping oscillation around its fundamental mode, it will degenerate into a single-mode model. For the above reason, a galloping piezoelectric energy harvester, as shown in Fig. 2, is often represented by a single-degree-of-freedom (SDOF) model.

The dynamic behavior of the lumped SDOF model of the GPEH subjected to an aerodynamic force is governed by the following equation.

$$M_{eff}\ddot{z}(L_b,t) + C_{eff}\dot{z}(L_b,t) + K_{eff}z(L_b,t) + \Theta V(t) = F_{galloping}(t)$$

where M_{eff}, C_{eff}, and K_{eff} are the equivalent mass, damping coefficient, and spring stiffness, respectively. L_b is the length of the cantilever beam. $z(L_b,t)$ is the translational tip displacement of the cantilever beam. $V(t)$ is the voltage across the piezoelectric transducer. Θ is system electromechanical coupling coefficient. The galloping force is often empirically represented by a polynomial function as:

$$F_{galloping}(t) = 0.5\rho S_c U^2 \sum\nolimits_{i=1}^{n} A_i \alpha^{i-1} \tag{9}$$

where α is the wind attack angle. By taking the rotation of the bluff body into account, the expression of the attack angle α should be rewritten as:

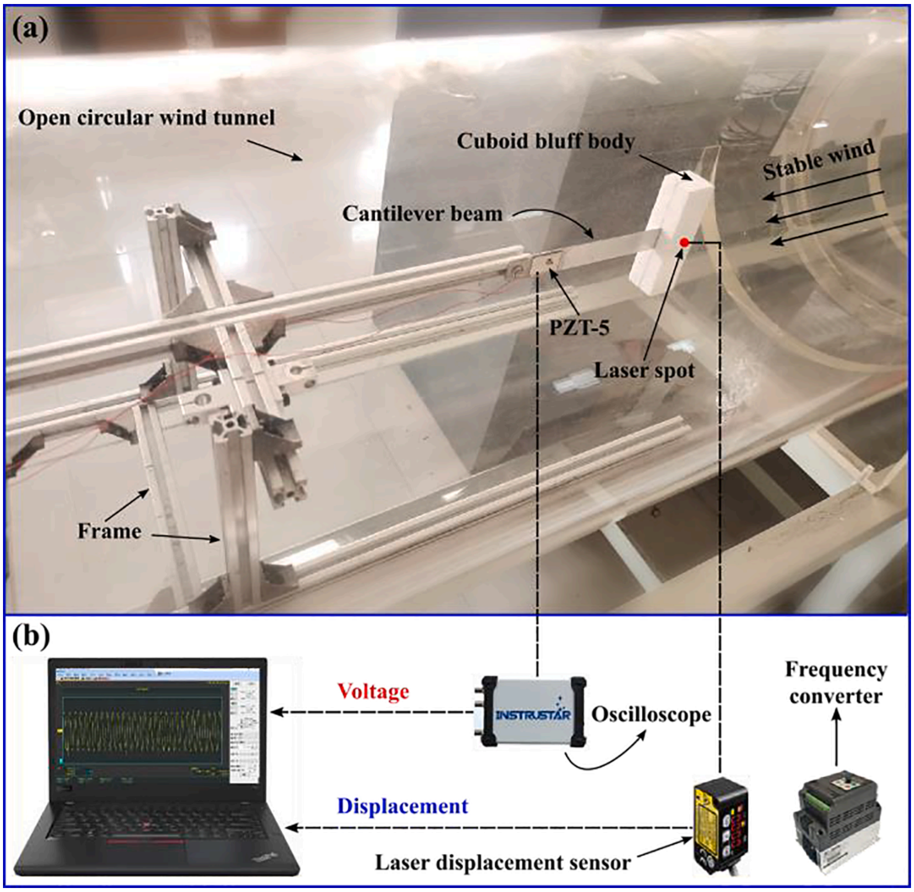

Fig. 10. (a) The GPEH prototype installed in the wind tunnel; (b) the data acquisition system.

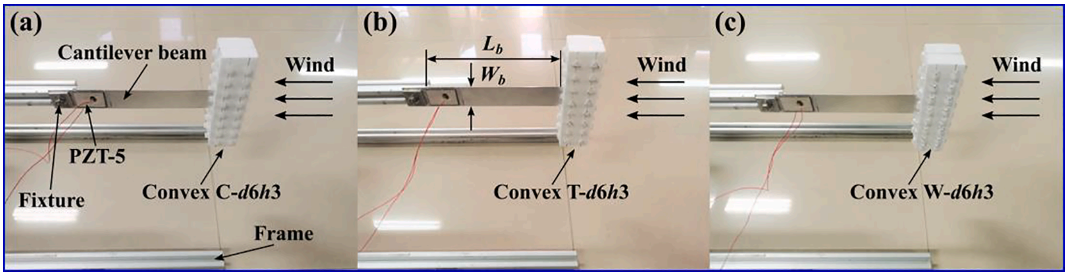

Fig. 11. The three GPEH prototypes with bluff bodies wrapped in different metasurfaces.

Table 4
The equivalent lumped parameters of the GPEH physical prototype.

Properties	Values/Units
M_{eff}	4.5×10^{-3} kg
f_n	9.76 Hz
ξ	0.0199
C_{eff}	0.0109 N/(m/s)
K_{eff}	16.834 N/m
C_p	20.38 (nF)
Θ	3.85×10^{-5} N/V

$$\alpha = \frac{\dot{z}(L_b, t)}{U} + z'(L_b, t) \tag{10}$$

where the rotation angle at the free end of the beam should be expressed as follows:

$$z'(L_b, t) = bz(L_b, t) \tag{11}$$

where b is the proportional coefficient between the rotation angle and the transverse displacement at the free end of the cantilever beam.

On the other hand, according to Kirchhoff's current law, the circuit governing equation can be written as:

$$I(t) + C_p\dot{V}(t) - \Theta\dot{z}(L_b, t) = 0 \tag{12}$$

where $I(t)$ is the current flows into the circuit and C_p is the clamped capacitance of the piezoelectric transducer. Assuming the piezoelectric transducer is shunted to a resistor R_L, the inflow current can be expressed as $I(t) = V(t)/R_L$.

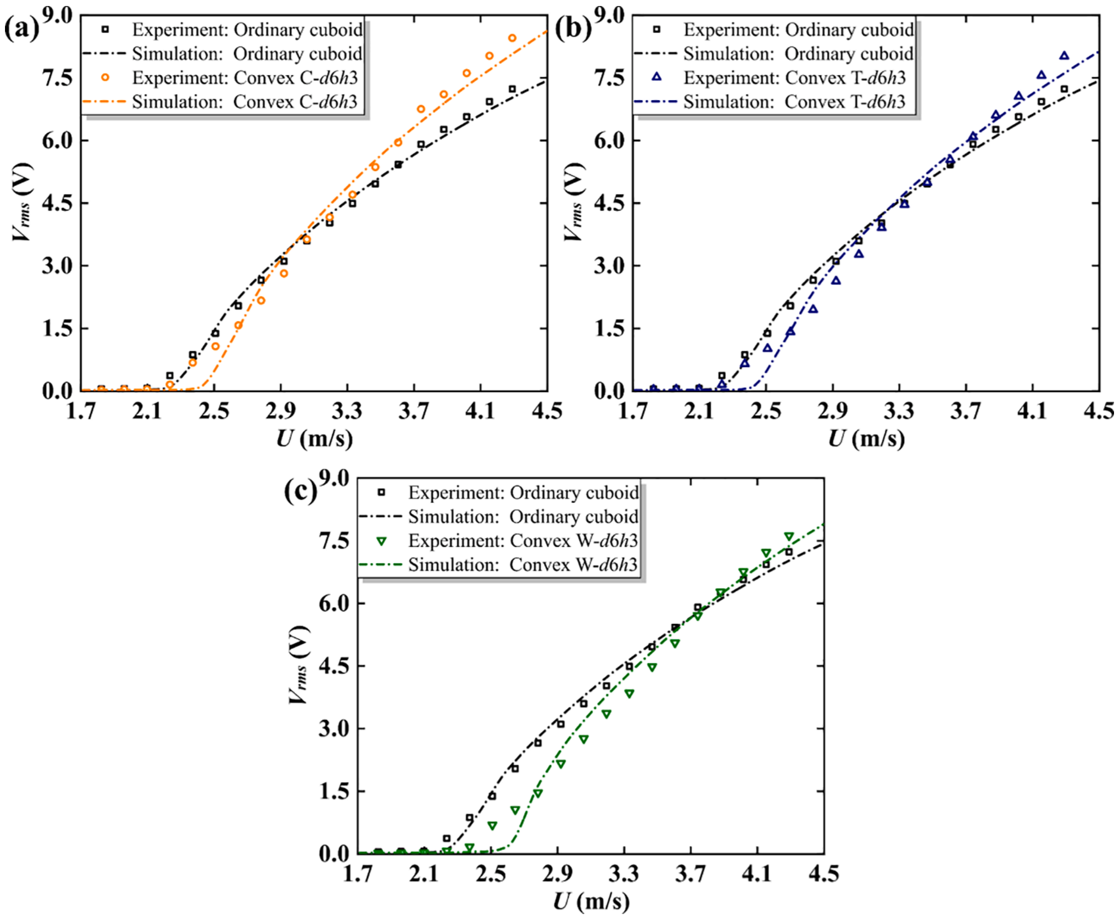

Fig. 12. Comparison of theoretical and experimental results for the three GPEHs using different bluff bodies.

Introducing the following variables:

$$q = \begin{Bmatrix} q_1 \\ q_2 \\ q_3 \end{Bmatrix} = \begin{Bmatrix} z(L_b, t) \\ \dot{z}(L_b, t) \\ V(t) \end{Bmatrix} \tag{13}$$

Eq. (8) and Eq. (12) can then be rewritten in the state-space form as:

$$\dot{q} = \begin{Bmatrix} \dot{q}_1 \\ \dot{q}_2 \\ \dot{q}_3 \end{Bmatrix} = \begin{Bmatrix} q_2 \\ -\dfrac{1}{M_{eff}}\left[C_{eff}q_2 + K_{eff}q_1 + \Theta q_3 - F_{galloping}(t)\right] \\ \dfrac{\Theta}{C_p}q_2 - \dfrac{q_3}{C_p R_L} \end{Bmatrix} \tag{14}$$

By numerically integrating Eq. (14) using such as the Runge-Kutta method, the dynamic response of the GPEH can be obtained.

2.2. Three-dimensional CFD model

In this section, the commercial software XFlow is adopted to perform the three-dimensional (3D) CFD simulation to determine the aerodynamic force applied on the bluff body for varying the wind attack angle. The kernel algorithm of XFlow is realized based on the Lattice-Boltzmann method (LBM). The LBM interprets the motion of the fluid as consecutive propagation and collision processes of particles. It does not need to solve the complex Navier-Stokes equations. Therefore, this method is very suitable for analyzing the fluid–structure interaction between coupled systems. The Boltzmann's transport equation is normally defined as follows:

$$n_i(r + D_i\Delta t, t + \Delta t) = n_i(r, t) + \Omega_i(n_1, \cdots, n_b) \tag{15}$$

where n_i stands for the statistical distribution function in the direction of i, based on the conservation of mass, linear momentum, and energy. D_i is the velocity component in one of the predetermined directions. Δt is the discrete time-step. Ω_i represents the collision operator, which computes a post-collision state conserving mass and linear momentum.

By introducing the Bhatnagar-Gross-Krook (BGK) model [52] proposed in 1954, the collision operator is expressed in the following formula:

$$\Omega_i = -\frac{1}{\tau}\left(n_i - n_i^{eq}\right) \tag{16}$$

where τ is the relaxation time. Fig. 3 shows the 27 discrete velocity directions that are usually used in a 3D element. The subscript i can take 0, 1, …, 26. n_i^{eq} is the local equilibrium function, which can be defined as:

$$n_i^{eq} = \omega_i \rho \left[1 + \frac{\overrightarrow{u}\cdot\overrightarrow{e}_i}{l_s^2} + \frac{\left(\overrightarrow{u}\cdot\overrightarrow{e}_i\right)^2}{2l_s^4} - \frac{\left(\overrightarrow{u}\right)^2}{2l_s^2}\right] \tag{17}$$

where $\overrightarrow{u}$ and ρ are the macroscopic velocity and the density of the fluid, respectively. ω_i is the weight parameter in the model, which can be found in previous work [53]. $\overrightarrow{e}_i$ is the discrete velocity that restricts the motion of the particles to the finite lattice sites. l_s is the lattice sound speed, and usually defined as:

$$l_s = (RT)^{\frac{1}{2}} \tag{18}$$

where R is the gas constant, and T is the macroscopic temperature.

According to the definition of the aerodynamic force, the pressure

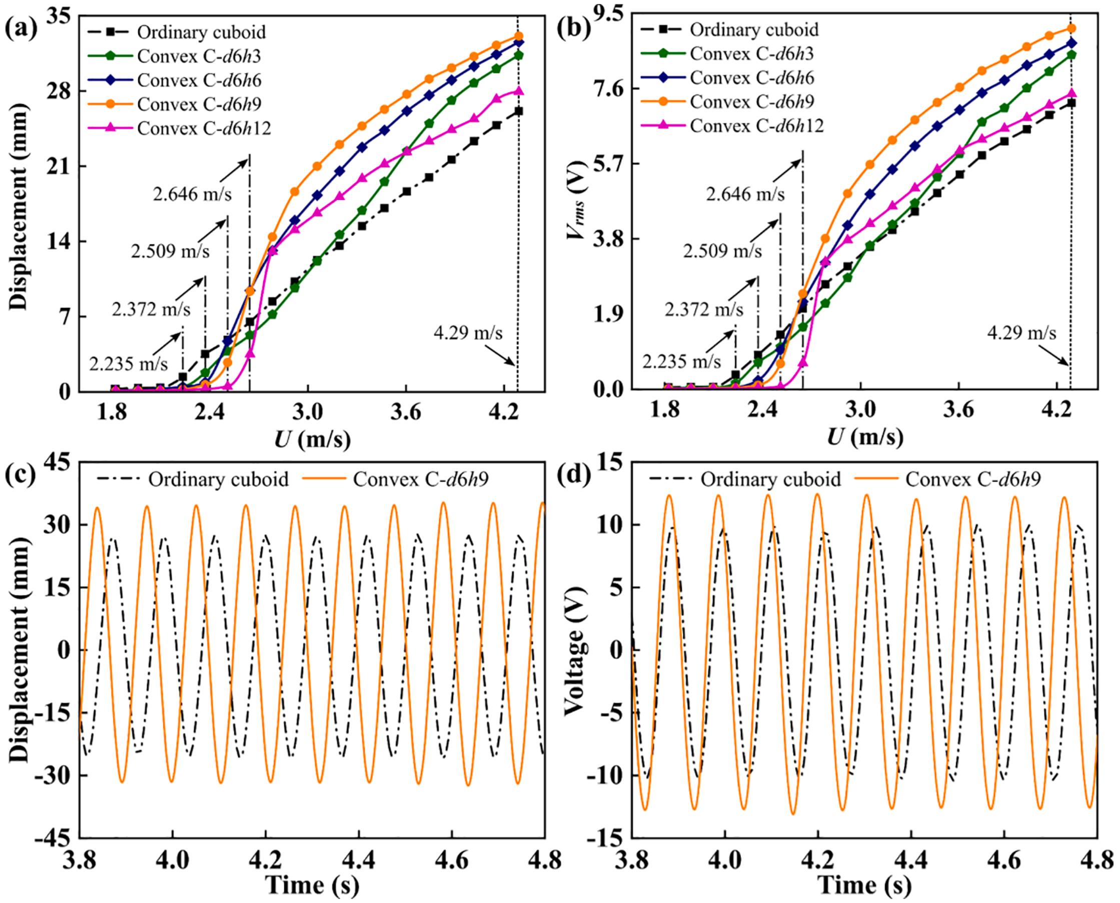

Fig. 13. The experimental results of the GPEHs using the bluff bodies wrapped in metasurfaces with convex cylinder ornaments of different heights: (a) vibration displacement versus wind speed; (b) RMS voltage output versus wind speed; time history responses of typical GPEH and Meta-GPEH with Convex C-*d*6*h*9 (c) displacement and (d) voltage at $U = 4.29$ m/s.

distribution around the bluff body needs to be first obtained. The lift and drag coefficients can then be computed by integrating the pressure over the bluff body surface. The macroscopic variables density term ρ and the velocity term $\rho\vec{u}$ are defined as:

$$\rho = \sum_i n_i = \sum_i n_i^{eq} \tag{19}$$

$$\rho\vec{u} = \sum_i D_i n_i = \sum_i D_i n_i^{eq} \tag{20}$$

The pressure could be obtained by the following equation:

$$P = \rho l_s^2 \tag{21}$$

According to the above principle, the lift and drag coefficients can be calculated by CFD simulations using XFlow. Before proceeding to the case study, the lattice size convergence is first assessed. The cuboid bluff body is taken as an example. The wind speed is assumed to be $U = 2.509$ m/s. Table 1 lists more detailed parameter values of the incoming flow. We test three different lattice sizes (0.0375*H*, 0.03125*H*, 0.02344*H*), which are referred to as crude, medium, and fine sizes, respectively. The near-wall lattice resolution is four times higher than the far-field lattice resolution. The settings of the computation domain and the boundary conditions are illustrated in Fig. 4. The left- and right-hand side boundaries are defined as the velocity inlet and the flow outlet, respectively. The remaining boundaries are set as stationary walls. The external single-phase and enforced incompressible model is adopted for simulating the flow.

The fixed automatic time-stepping mode is applied, and the time step is 9.21659e-5 s. For the given parameters, the Reynolds number (i.e., $Re = \rho UH/\nu$) is calculated to be around 5400, which indicates a turbulent flow situation. Therefore, the Smagorinsky turbulence model implemented in XFlow is adopted to carry out the turbulence simulation [54]. Fig. 5 shows the time history responses of the drag coefficient computed using the crude, medium, and fine lattice sizes, respectively. The root-mean-square (RMS) value of the lift coefficient C_{Lrms} and the mean value of the drag coefficient C_D are listed in Table 2. It is noted that for the lattice numbers of 1,516,800 and 3,448,960, the computational results of the C_{Lrms} and C_D are close. Thus, the lattice number of 1,516,800 is chosen in the following simulations for the sake of computing cost efficiency.

As the lattice independence has been successfully verified, the aerodynamic force applied on the different bluff bodies is simulated based on the quasi-steady hypothesis. The quasi-steady-state (QSS) theory is valid if the time scale of the structural oscillation characteristics of the galloping $2\pi/\omega_n$ is much larger than the characteristic time scale of the flow passing the bluff body H/U [55]. Fig. 6 presents the cross-section shape of a three-dimensional cuboid. The clockwise direction indicates a positive angle of attack. The total aerodynamic force on the three-dimensional cuboid can be decomposed into the lift force and the drag force:

$$F_L = 0.5\rho S_c U^2 C_L \tag{22}$$

$$F_D = 0.5\rho S_c U^2 C_D \tag{23}$$

F_z is the vector resultant of the lift and drag forces in the vertical direction. It is expressed as follows:

$$F_z = -F_L\cos\alpha - F_D\sin\alpha = 0.5\rho S_{cro} U^2 C_{Fz} \tag{24}$$

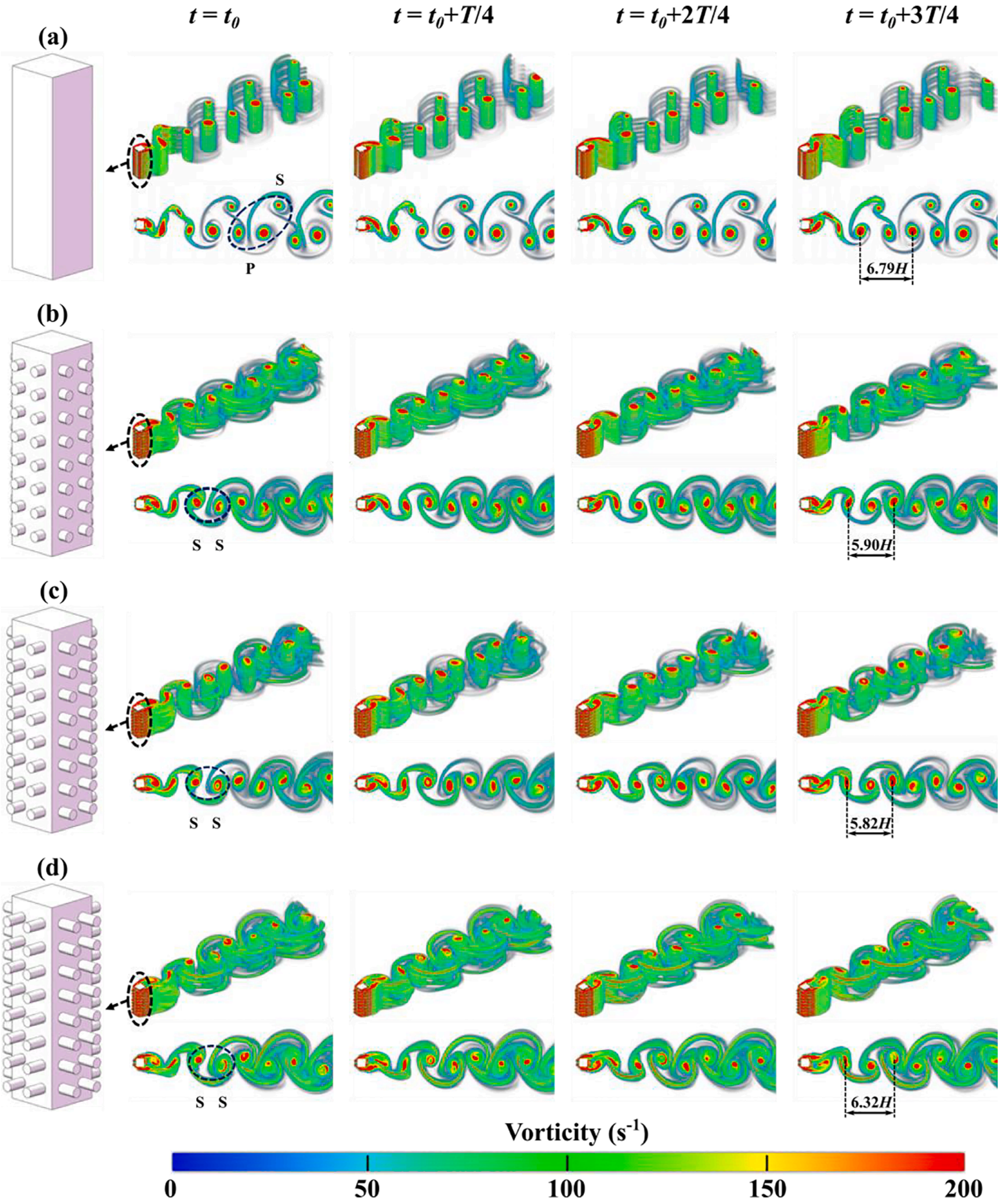

Fig. 14. Vorticity contours obtained from 3D CFD simulations to illustrate the vortex shedding processes around: (a) the ordinary cuboid bluff body; (b) the bluff body wrapped in the metasurface with Convex C-*d*6*h*6 ornament; (c) the bluff body wrapped in the metasurface with Convex C-*d*6*h*9 ornament; (d) the bluff body wrapped in the metasurface with Convex C-*d*6*h*12 ornament.

where the vertical force coefficient can be expressed using the following formula:

$$C_{Fz} = -\frac{U_{rel}^2}{U^2}(C_L\cos\alpha + C_D\sin\alpha) = -(C_L + C_D\tan\alpha)\sec\alpha \tag{25}$$

where C_L and C_D are the mean lift coefficient and mean drag coefficient, respectively. According to the QSS theory and based on Eq. (25), C_{Fz} at different wind attack angles can be obtained by 3D CFD simulations. The calculation results for the cuboid bluff body are plotted in Fig. 7 as a collection of discrete points. Ng et al. [56] demonstrated that the use of a seventh-order polynomial is already sufficient for describing the nonlinear relationship between the wind attack angle and the aerodynamic force coefficient. Thus, Eq. (26) is adopted in this present study to fit the simulation data shown in Fig. 7.

$$C_{Fz} = A_1\alpha + A_3\alpha^3 + A_5\alpha^5 + A_7\alpha^7 \tag{26}$$

Using the least-squares method, the coefficients A_i can be determined based on the simulation data. In Fig. 7, the 3D CFD vorticity contour at the angle of attack corresponding to the maximum C_{Fz} is also illustrated.

As presented in Fig. 7, C_{Fz} first increases then decreases with the increase of attack angle α, and finally becomes negative. It can be seen that the instability criterion $\partial C_{Fz}/\partial\alpha$ greater than 0 for galloping is satisfied, which requires coefficient A_1 to be positive and A_3 to be negative [57]. The validated 3D CFD method is then used to compute C_{Fz} for the three metasurface-wrapped bluff bodies, as shown in Fig. 8. Uniform ornaments in the shape of a convex cylinder (CC), convex triprism (CT), and convex wedge (CW) are periodically distributed on the three metasurfaces. The periodicities of the three types of convex ornaments are the same: eight rows and two columns on each side of the

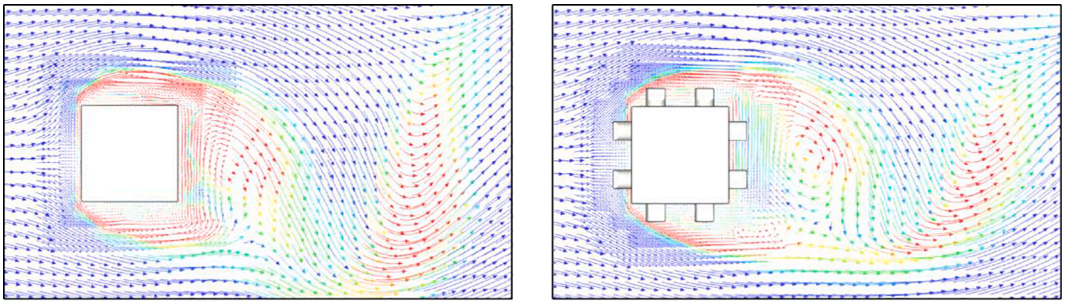

(a) Ordinary cuboid (b) Convex C-*d*6*h*6

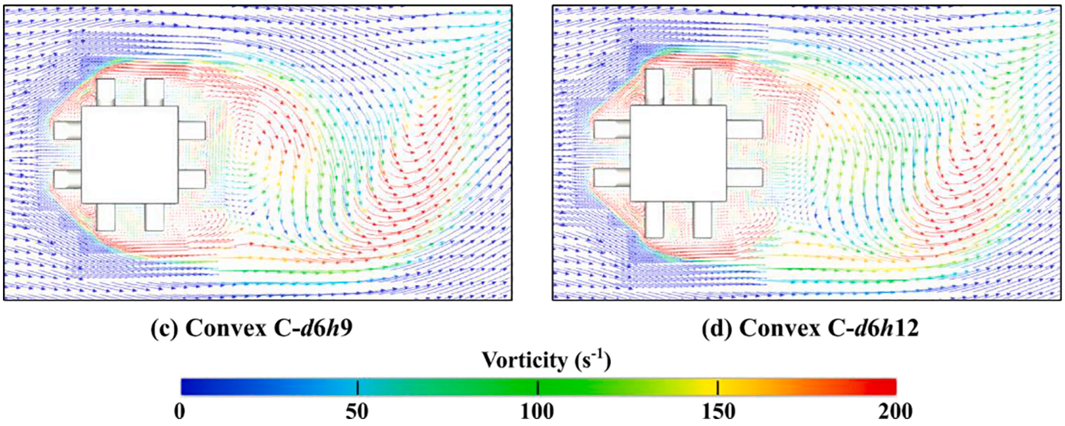

(c) Convex C-*d*6*h*9 (d) Convex C-*d*6*h*12

Fig. 15. Vorticity vectors obtained from 3D CFD simulations to illustrate the leading-edge flow around: (a) the ordinary cuboid bluff body; (b) the bluff body wrapped in the metasurface with Convex C-*d*6*h*6 ornament; (c) the bluff body wrapped in the metasurface with Convex C-*d*6*h*9 ornament; (d) the bluff body wrapped in the metasurface with Convex C-*d*6*h*12 ornament.

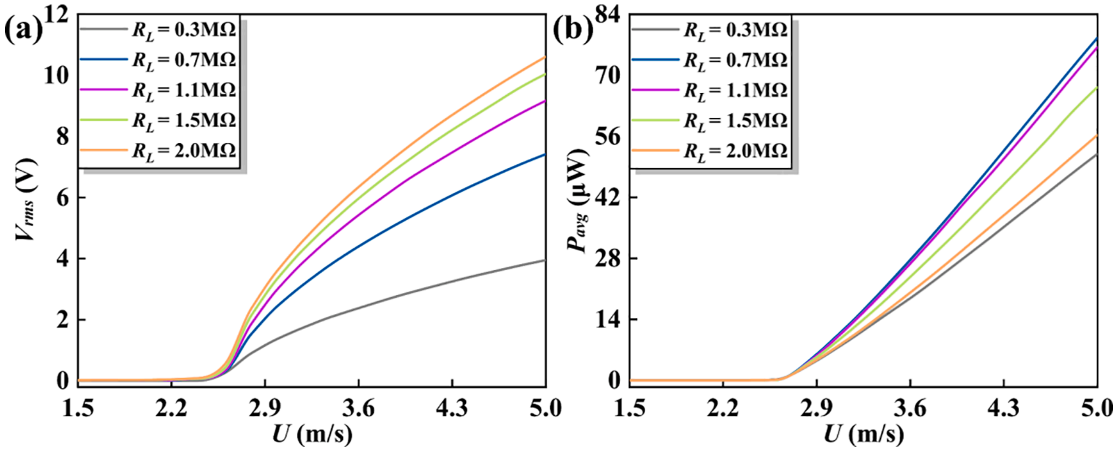

Fig. 16. (a) The RMS output voltage and (b) the averaged power versus wind speed under different electrical load resistances.

cuboid bluff body. The characteristic width d and the height of the convex ornaments are 6 mm and 3 mm, respectively. Fig. 9 presents the results of the aerodynamic force coefficients C_{Fz} for the three bluff bodies wrapped in different metasurfaces.

Based on the simulation data (a collection of circular or triangular points in Fig. 9), the aerodynamic force coefficients for the three bluff bodies wrapped in metasurfaces are identified and listed in Table 3. From Table 3, one knows that the linear coefficient A_1 for the ordinary bluff body is the largest, indicating that the typical GPEH has a greater tendency to lose stability. Thus, it can be inferred that the typical GPEH should have the lowest cut-in wind speed. On the other hand, the cubic coefficients A_3 for the three Meta-GPEHs are smaller than that of the typical GPEH. Hence, we can deduce that the cubic coefficients A_3 for the three Meta-GPEHs have weaker constraints on their oscillation amplitudes. In other words, the three Meta-GPEHs may attain larger oscillation amplitudes and produce larger voltage outputs when the wind speed is large.

3. Design prototypes and experimental setup

Fig. 10 demonstrates the physical prototype and the experimental setup. The cantilever beam and the bluff body of the GPEH are made of aluminum and foam, respectively. The GPEH is mounted on a fixed frame. The whole system is placed in an open circular wind tunnel with a diameter of 0.4 m. A honeycomb device is installed at the right-hand side of the wind tunnel to straighten the air flow by minimizing the lateral velocity components caused by swirling motion. The wind speed in the wind tunnel can be controlled by changing the fan rotation speed,

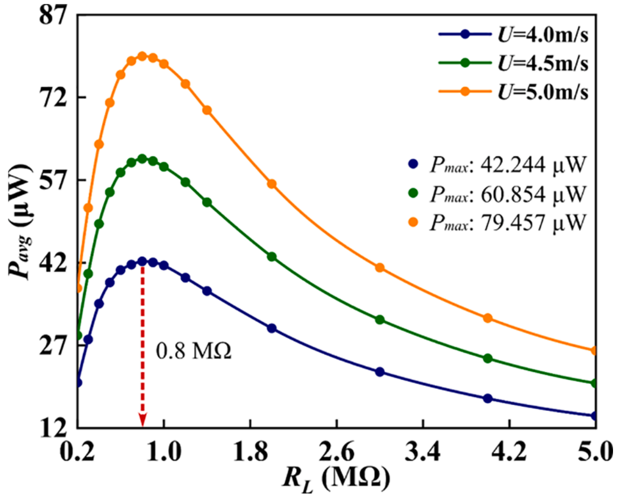

Fig. 17. The averaged power versus the electrical load resistances under different wind speeds.

which is realized by adjusting the frequency converter. To be more specific, the conversion relationship between wind speed and frequency is $U = 0.137f + 0.18$. A hot-wire anemometer (405i, Testo Co, USA) is used to calibrate the wind speed with a resolution of 0.001 m/s. Fig. 10 (b) shows the data acquisition system. The voltage generated by the PZT-5 transducer is recorded by a dual-channel oscilloscope (ISDS220B), and its bandwidth, sampling rate, and vertical resolution are 60 MHz, 200 MS/s, and 8 bits, respectively. The vibration displacement of the bluff body is measured by a laser sensor (Panasonic: HG-C1400), which has a repeatability resolution of 300 μm. The laser spot strikes at the center of the bluff body. Fig. 11 presents the three GPEH prototypes with bluff bodies wrapped in different metasurfaces. It should be noted that the weight of the GPEH prototype changes when the ordinary cuboid bluff body is wrapped in a different metasurface. Therefore, in the experiment, suitable small mass blocks are added inside the bluff bodies to compensate for the weight difference to guarantee the comparison fairness. It is worth mentioning that in the following experiment, the working wind speed range is 1.824 ~ 4.29 m/s.

According to the SDOF modelling method, the effective mass M_{eff} is the weighted sum of the masses of the metasurface-wrapped bluff body, the piezoelectric transducer, and the cantilever beam. The natural frequency f_n can be obtained from the free decay test. The damping ratio ξ can be determined using the logarithmic decrement method based on the free decay test result. The effective damping can thus be calculated as $C_{eff} = 4\pi f_n \xi M_{eff}$. The effective spring stiffness is determined by $K_{eff} = (2\pi f_n)^2 M_{eff}$. The equivalent lumped parameters of the GPEH prototype are listed in Table 4. It is worth noting that the equivalent lumped parameters of the three Meta-GPEHs are the same as those of the ordinary GPEH.

4. Experimental results and discussion

Fig. 12 compares the theoretical and experimental results of the root-mean-square (RMS) output voltage V_{rms} from the GPEHs. The theoretical results are overall in agreement with the experimental data over the wind speed range (1.7 ~ 4.5 m/s). The slight discrepancy may be due to the following two reasons. First, the CFD simulation normally can not be absolutely accurate, and there often exists a prediction error as compared to the experimental test. Second, the aerodynamic force is obtained by using a seventh-order polynomial function to fit the CFD simulation data. Therefore, the curving fitting operation also causes additional errors. As shown in Fig. 9, when the wind attack angle is small, the aerodynamic force coefficient calculated using the seventh-order polynomial function is slightly larger than the simulation result. In contrast, when the wind attack angle is large, the aerodynamic force coefficient calculated using the seventh-order polynomial function is slightly smaller than the simulation result. This generally matches the discrepancy revealed in Fig. 12. The experimental data are distributed on both sides of the theoretical curves. The experimental and theoretical results of the typical GPEH with an ordinary cuboid bluff body are also provided in Fig. 12 for comparison. It can be found that though the cut-in wind speeds of Meta-GPEHs are increased compared to that of the typical GPEH, once the wind speed is sufficiently high, Meta-GPEHs can produce larger voltage outputs. As aforementioned when discussing Eqs. (7a) and (7b), the linear coefficient A_1 implies the stability condition of the GPEH, thus its cut-in wind speed. The above phenomenon agrees well with the previous discussion on the fitting coefficients of C_{Fz} listed in Table 3.

From the above experimental results, one notes that compared to the typical GPEH using an ordinary cuboid bluff body, the Meta-GPEH using a bluff body wrapped in the metasurface with convex cylinder ornaments exhibits an enhanced energy harvesting performance: the voltage output is significantly improved, though the cut-in wind speed is slightly increased. It is, thus, motivated to perform a further study to investigate the influences of the parameters of the convex cylinders that constitute the metasurface. The diameter of the cylinder is fixed the same as 6 mm. The height of the cylinder is varied. Three bluff bodies wrapped in the metasurfaces with different ornaments, namely Convex C-$d6h6$, Convex C-$d6h9$, and Convex C-$d6h12$, are investigated. $dXhY$ denotes that the diameter and the height of the ornament are, respectively, X mm and Y mm. Fig. 13 presents the experimental results of the Meta-GPEHs with different convex cylinder heights. The result of the typical GPEH is also

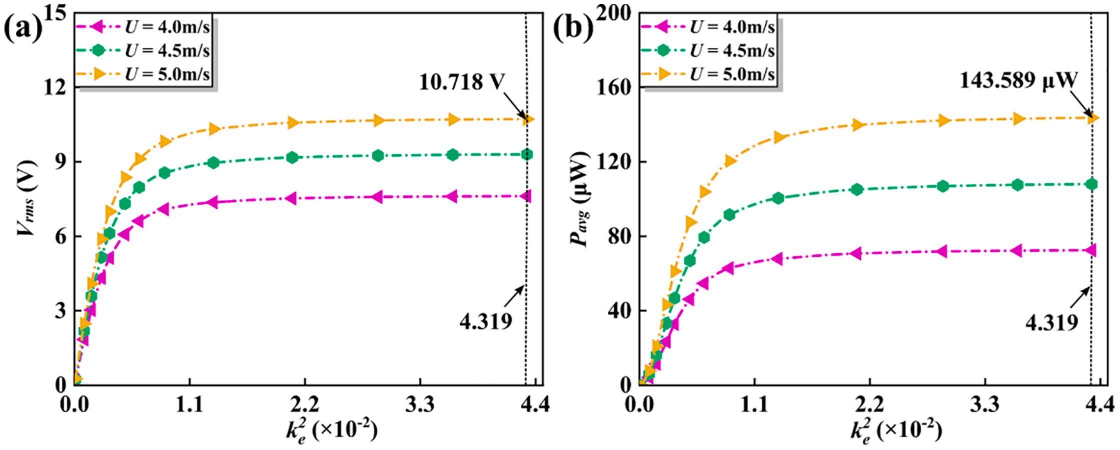

Fig. 18. (a) The RMS output voltage and (b) the averaged power versus the electromechanical coupling strength k_e^2 under different wind speeds.

provided for comparison. It can be observed from Fig. 13 (a) that under the wind speed of $U = 4.29$ m/s, the displacement amplitude of the typical GPEH is about 26.11 mm. Under the same wind speed, for the convex cylinder height of $h = 3$, 6, 9, and 12, the maximum displacement amplitudes of the Meta-GPEHs are, respectively, 31.32 mm, 32.55 mm, 33.11 mm, and 27.94 mm. As plotted in Fig. 13 (b), the output voltage amplitude of the typical GPEH is about 7.23 V. By changing the convex height of h to 3, 6, 9, and 12 mm, the output voltage amplitude of the Meta-GPEH correspondingly becomes 8.45 V, 8.74 V, 9.12 V, and 7.46 V. It is noted that the displacement and output voltage amplitudes first increase then decrease with the increase of the convex height h. Among the four samples, the Convex C-*d*6*h*9 yields the best performance: the displacement and output voltage amplitudes of the Meta-GPEH are increased by 26.81% and 26.14%, respectively, compared to the typical GPEH.

The time history responses of typical GPEH and Meta-GPEH with Convex C-*d*6*h*9 at $U = 4.29$ m/s are shown in Fig. 13 (c) and (d). At this wind speed, both the vibration amplitude and the output voltage reach their maximum values. The oscillations of the two energy harvesters with different bluff bodies are single-period. It can be clearly observed that the displacement/voltage amplitude of the Meta-GPEH with Convex C-*d*6*h*9 is significantly larger.

5. Further simulation and theoretical analysis

5.1. Interpretation of the flow field

The vortex shedding processes are analyzed to further unveil the mechanism of the improvements brought by the metasurfaces. Fig. 14 presents the CFD simulation obtained vorticity contours around convex cylinder bluff bodies with different ornament height h and the ordinary cuboid bluff body. T is the time of a vortex shedding cycle. The variation of vortex shedding frequency can be illustrated by the streamwise distance between two adjacent vortices shed from the same shear layer [58]. In Fig. 14, the existence of metasurface structures makes the vortex shedding mode change from “P + S” type to “2S” type [59]. For the bluff body wrapped in the metasurface, when $h = 6$, 9, and 12, the streamwise distances between two adjacent vortices are 5.90H, 5.82H, and 6.32H, respectively. They are all smaller than that of the ordinary cuboid bluff body (6.79H), indicating the increase of the vortex shedding frequency. The densified vortex shedding contributes to the increase of the aerodynamic force applied on the bluff body, as well as the output voltage amplitude from the piezoelectric transducer. Among the three convex cylinder bluff bodies, the streamwise distance between two adjacent vortices of the Convex C-*d*6*h*9 bluff body is the smallest, which well explains why the corresponding Meta-GPEH produces the largest output voltage amplitude.

Fig. 15 presents the vorticity vectors obtained from 3D CFD simulations around bluff bodies with different characteristics to illustrate the variation near the leading-edge flow field. By comparing Fig. 15 (a)–(d), one can see that the existence of metasurfaces influences the flow field near the bluff bodies. Compared with the ordinary cuboid bluff body, with the increase of the convex height h, the vortex phenomenon begins to appear on both sides of the bluff body upstream, resulting in a faster boundary layer separation near the bluff body and a faster vortex shedding process. However, as the convex cylinder height h is 12 mm, small vortices are formed between the protrusion structures, which indicates that when the convex height is too lager, the boundary layer separation could be delayed to a certain extent. Thus, the vortex shedding will slow down, and the generated vortices will be weaker, so the improvement of energy harvesting performance will be suppressed. This is consistent with the experimental result.

5.2. Parametric analysis

This section aims to explore the means to further improve the energy harvesting performance from the electromechanical perspective. To this end, the influences of the electrical load resistance and the electromechanical coupling strength on the performance of the energy harvester are investigated. Since the theoretical model has already been validated in Section 4, the following parametric study is performed based on the theoretical model. We take the galloping energy harvester using the bluff body wrapped in the metasurface with Convex C-*d*6*h*3 ornaments as an example for the following parametric analysis. k_e^2 is a dimensionless parameter that is introduced to indicate the electromechanical coupling strength. The averaged power is used to assess the energy harvesting performance.

$$k_e^2 = \frac{\Theta^2}{C_p K_{eff}} \tag{27}$$

$$P_{avg} = \frac{V_{rms}^2}{R_L} \tag{28}$$

Fig. 16 shows the RMS output voltage and the averaged power under different electrical load resistances. It can be seen from Fig. 16 (a) that under the same wind speed, the RMS output voltage is proportional to the R_L, and the increasing rate gradually slows down. When $R_L = 2.0$ MΩ, the maximum output voltage can reach 10.612 V. While, as can be found from Fig. 16 (b), the average power first increases and then decreases with the increase of the electrical load resistances, indicating that there is an optimal electrical load resistance in the range of 0.7 ~ 1.1 MΩ. Therefore, to further determine the optimal electrical load resistance, Fig. 17 presents the relationship between the averaged power and the electrical load resistances under different wind speeds. One can see that under each wind speed, the averaged power has a peak value and the optimal $R_{L0} = 0.8$ MΩ.

The electromechanical coupling strength is also one of the important factors that affect the energy harvesting performance. With the change of the electromechanical coupling strength k_e^2, the variations of the RMS output voltage and the averaged power under different wind speeds are shown in Fig. 18. It is worth noting that the change of the electromechanical coupling strength k_e^2 is realized by changing the capacitance, while the system electromechanical coupling coefficient Θ remains constant. The results show that the RMS output voltage and the averaged power increase with the increase of k_e^2 and converge to constant values. When $k_e^2 = 4.319 \times 10^{-2}$ and $U = 5.0$ m/s, the maximum RMS output voltage is 10.718 V, and the maximum averaged power is 143.589 μW. Hence, it is learned that an appropriate increase of the electromechanical coupling strength helps to improve the energy harvesting performance.

6. Conclusions

In summary, we have demonstrated that wrapping bluff bodies in metasurfaces can potentially improve the galloping energy harvesting performance. A general theoretical model has been developed for predicting the performance of a galloping piezoelectric energy harvester using a universal bluff body. The aerodynamic force in the theoretical model has been represented by a seventh-order polynomial function determined by fitting the data from 3D CFD simulations. Three metasurfaces distributed with convex cylinder, tri-prim, and wedge ornaments have been designed. Physical prototypes have been fabricated. The experimental test results have validated the theoretical model. The synergy of three-dimensional CFD simulation and theoretical model is specifically for the modeling and computation of the proposed galloping system with metasurfaces. The results show that the metasurface can significantly change the aerodynamic characteristics of the bluff body. Wrapping the bluff body in the metasurface with convex cylinder ornaments has been found to result in a significant increase in the output voltage amplitude.

A further experimental investigation has shown that when the convex cylinder ornaments are designed with a diameter of 6 mm and height of 9 mm, the maximum vibration displacement and maximum output voltage of the proposed galloping piezoelectric energy harvester can be increased by 26.81% and 26.14%, respectively, compared to the typical GPEH. Vorticity contours around the bluff bodies have been simulated to provide insights into the vortex shedding processes for explaining the improvements brought by metasurfaces. It has been observed that the existence of metasurfaces could fasten the boundary layer separation and intensify the vortex shedding process, resulting in the increase of the aerodynamic force applied on the bluff body.

Besides the bluff body, we have also attempted to improve the energy harvesting performance by manipulating the electrical domain settings. A parametric study based on the theoretical model has revealed the effects of the load resistance and the electromechanical coupling strength on the galloping energy harvesting performance. It is learned that by considerably increasing the electromechanical coupling strength and tuning the load resistance to the optimal value, the power output can be significantly increased. However, when the electromechanical coupling strength increases to a certain extent, the power output will reach the saturation state, and the coupling strength is extremely large. Since the cost of a strong coupling coefficient piezoelectric element is usually high, it is suggested to choose a piezoelectric element with a moderate coupling coefficient from the perspective of economic benefit.

In the future, on the one hand, efforts may be devoted to further optimizing the metasurface-based galloping energy harvester. A systematic optimization scheme may be developed to select the most appropriate metasurface and determine the optimal parameters for achieving the best energy harvesting performance. On the other hand, one can dedicate to exploring the feasibility of using metasurfaces to realize the coupling between galloping and vortex-induced vibration phenomena for promoting energy harvesting performance.

CRediT authorship contribution statement

Junlei Wang: Conceptualization, Formal analysis, Investigation, Methodology, Resources, Writing - original draft, Funding acquisition. **Shaokang Sun:** Data curation, Software, Writing - original draft. **Guobiao Hu:** Conceptualization, Supervision, Formal analysis, Investigation, Writing - review & editing. **Yaowen Yang:** Investigation, Writing - review & editing. **Lihua Tang:** Investigation, Writing - review & editing. **Pan Li:** Supervision, Investigation, Writing - review & editing. **Guojie Zhang:** Investigation, Writing - review & editing.

Declaration of Competing Interest

The authors declare that they have no known competing financial interests or personal relationships that could have appeared to influence the work reported in this paper.

Acknowledgments

This work was supported by the National Natural Science Foundation of China (Grant No.: 51977196), China Postdoctoral Science Foundation (2020T130557) and Soyotec Technologies Co., Ltd. (Beijing) on XFlow Software.

References

[1] Fu H, Mei X, Yurchenko D, Zhou S, Theodossiades S, Nakano K, et al. Rotational energy harvesting for self-powered sensing. Joule 2021;5(5):1074–118.

[2] Liu H, Zhong J, Lee C, Lee S-W, Lin L. A comprehensive review on piezoelectric energy harvesting technology: materials, mechanisms, and applications. Appl Phys Rev 2018;5(4):041306. https://doi.org/10.1063/1.5074184.

[3] Lai ZH, Wang JL, Zhang CL, Zhang GQ, Yurchenko D. Harvest wind energy from a vibro-impact DEG embedded into a bluff body. Energy Convers Manage 2019;199:13.

[4] Zhang ZH, Wang SY, Kan JW, Hu WJ, Chen ZF, Xu HL. A pneumatic piezoelectric vibration energy harvester based on the compressed air-transducer-structure interaction. Energy Convers Manage 2020;213:11.

[5] Zuo W, Li QQ, He Z, Li YW. Numerical investigations on thermal performance enhancement of hydrogen-fueled micro planar combustors with injectors for micro-thermophotovoltaic applications. Energy 2020;194:14.

[6] Xu WH, Zhang SH, Ma YX, Liu B. Fluid forces acting on three and four long side-by-side flexible cylinders undergoing flow-induced vibration(FIV). Mar Struct 2021;75:19.

[7] Stamatellou A-M, Kalfas AI. Testing of piezoelectric energy harvesters isolated from base vibrations. Energy Convers Manage 2019;196:717–28.

[8] Zhao DL, Hu XY, Tan T, Yan ZM, Zhang WM. Piezoelectric galloping energy harvesting enhanced by topological equivalent aerodynamic design. Energy Convers Manage 2020;222:11.

[9] Lallart M, Lombardi G. Synchronized Switch Harvesting on ElectroMagnetic System: a nonlinear technique for hybrid energy harvesting based on active inductance. Energy Convers Manage 2020;203:12.

[10] Peng Y, Xu Z, Wang M, Li Z, Peng J, Luo J, et al. Investigation of frequency-up conversion effect on the performance improvement of stack-based piezoelectric generators. Renew Energy 2021;172:551–63.

[11] Tao K, Chen Z, Yi H, Zhang R, Shen Q, Wu J, et al. Hierarchical honeycomb-structured electret/triboelectric nanogenerator for biomechanical and morphing wing energy harvesting. Nano-Micro Lett 2021;13(1). https://doi.org/10.1007/s40820-021-00644-0.

[12] Zhao L-C, Zou H-X, Yan Ge, Liu F-R, Tan T, Zhang W-M, et al. A water-proof magnetically coupled piezoelectric-electromagnetic hybrid wind energy harvester. Appl Energy 2019;239:735–46.

[13] Chen W-L, Zhang Q-Q, Li H, Hu H. An experimental investigation on vortex induced vibration of a flexible inclined cable under a shear flow. J Fluids Struct 2015;54:297–311.

[14] Zhao X, Cai J, Guo Y, Li C, Wang J, Zheng H. Modeling and experimental investigation of an AA-sized electromagnetic generator for harvesting energy from human motion. Smart Mater Struct 2018;27(8):085008. https://doi.org/10.1088/1361-665X/aacdc4.

[15] Bo LD, Gardonio P, Turco E. Analysis and scaling study of vibration energy harvesting with reactive electromagnetic and piezoelectric transducers. J Sound Vib 2020;484:28.

[16] Zhang LB, Meng B, Xia Y, Deng ZM, Dai HL, Hagedorn P, et al. Galloping triboelectric nanogenerator for energy harvesting under low wind speed. Nano Energy 2020;70:11.

[17] Yar A, Karabiber A, Ozen A, Ozel F, Coskun S. Flexible nanofiber based triboelectric nanogenerators with high power conversion. Renew Energy 2020;162:1428–37.

[18] Wang Q, Zou H-X, Zhao L-C, Li M, Wei K-X, Huang L-P, et al. A synergetic hybrid mechanism of piezoelectric and triboelectric for galloping wind energy harvesting. Appl Phys Lett 2020;117(4):043902. https://doi.org/10.1063/5.0014484.

[19] Khazaee M, Rosendahl L, Rezania A. A comprehensive electromechanically coupled model for nonuniform piezoelectric energy harvesting composite laminates. Mech Syst Sig Process 2020;145:26.

[20] Hu G, Wang J, Tang L. A comb-like beam based piezoelectric system for galloping energy harvesting. Mech Syst Sig Process 2021;150:107301. https://doi.org/10.1016/j.ymssp.2020.107301.

[21] Naderi A, Fakher M, Hosseini-Hashemi S. On the local/nonlocal piezoelectric nanobeams: vibration, buckling, and energy harvesting. Mech Syst Sig Process 2021;151:107432. https://doi.org/10.1016/j.ymssp.2020.107432.

[22] Wang JL, Gu SH, Zhang CY, Hu GB, Chen G, Yang K, et al. Hybrid wind energy scavenging by coupling vortex-induced vibrations and galloping. Energy Convers Manage 2020;213:11.

[23] Yang ZS, Tang LH, Yu LD, Tao K, Aw K. Modelling and analysis of an out-of-plane electret-based vibration energy harvester with AC and DC circuits. Mech Syst Sig Process 2020;140:15.

[24] Guseinov NR, Ilyin AM. Electrostatic energy analyzer for nanotechnology applications. J Electron Spectrosc Relat Phenom 2021;246:6.

[25] Chen Z, Xia Y, He J, Xiong Y, Wang G. Elastic-electro-mechanical modeling and analysis of piezoelectric metamaterial plate with a self-powered synchronized charge extraction circuit for vibration energy harvesting. Mech Syst Sig Process 2020;143:106824.

[26] Lai Z, Wang S, Zhu L, Zhang G, Wang J, Yang K, et al. A hybrid piezo-dielectric wind energy harvester for high-performance vortex-induced vibration energy harvesting. Mech Syst Sig Process 2021;150:107212. https://doi.org/10.1016/j.ymssp.2020.107212.

[27] Wang JL, Geng LF, Ding L, Zhu HJ, Yurchenko D. The state-of-the-art review on energy harvesting from flow-induced vibrations. Appl Energy 2020;267:17.

[28] Laima S, Li H, Chen W, Li F. Investigation and control of vortex-induced vibration of twin box girders. J Fluids Struct 2013;39:205–21.

[29] Xu W, Zhang S, Ma Y, Liu B, Wang J. A study on the FIV hydrodynamic force coefficients of two staggered flexible cylinders via an inverse method. Ocean Eng 2021;219:108272. https://doi.org/10.1016/j.oceaneng.2020.108272.

[30] Wang JL, Sun SK, Tang LH, Hu GB, Liang JR. On the use of metasurface for Vortex-Induced vibration suppression or energy harvesting. Energy Convers Manage 2021;235:14.

[31] Bashir M, Rajendran P, Khan SA, Iop. Energy harvesting from aerodynamic instabilities: current prospect and future trends. In: International Conference on Advances in Manufacturing and Materials Engineering, 2018.

[32] Alhadidi AH, Daqaq MF. A broadband bi-stable flow energy harvester based on the wake-galloping phenomenon. Appl Phys Lett 2016;109(3):033904. https://doi.org/10.1063/1.4959181.

[33] Dai HL, Yang YW, Abdelkefi A, Wang L. Nonlinear analysis and characteristics of inductive galloping energy harvesters. Commun Nonlinear Sci Numer Simul 2018;59:580–91.

[34] Tan T, Yan Z. Optimization study on inductive-resistive circuit for broadband piezoelectric energy harvesters. AIP Adv 2017;7(3):035318. https://doi.org/10.1063/1.4979508.

[35] Zhao L, Yang Y. Comparison of four electrical interfacing circuits in wind energy harvesting. Sens Actuat A-Phys 2017;261:117–29.

[36] Yang Y, Zhao L, Tang L. Comparative study of tip cross-sections for efficient galloping energy harvesting. Appl Phys Lett 2013;102(6):064105. https://doi.org/10.1063/1.4792737.

[37] Zhang L, Meng B, Xia Y, Deng Z, Dai H, Hagedorn P, et al. Galloping triboelectric nanogenerator for energy harvesting under low wind speed. Nano Energy 2020;70:104477.

[38] Hu G, Tse KT, Kwok KCS. Enhanced performance of wind energy harvester by aerodynamic treatment of a square prism. Appl Phys Lett 2016;108(12):123901. https://doi.org/10.1063/1.4944555.

[39] Noel J, Yadav R, Li G, Daqaq MF. Improving the performance of galloping micro-power generators by passively manipulating the trailing edge. Appl Phys Lett 2018;112(8):083503. https://doi.org/10.1063/1.5016102.

[40] Zhu H, Zhao Y, Zhou T. CFD analysis of energy harvesting from flow induced vibration of a circular cylinder with an attached free-to-rotate pentagram impeller. Appl Energy 2018;212:304–21.

[41] Wang J, Zhou S, Zhang Z, Yurchenko D. High-performance piezoelectric wind energy harvester with Y-shaped attachments. Energy Convers Manage 2019;181:645–52.

[42] Umul YZ. Diffraction of electromagnetic waves by an anomalously transmitting metasurface half-plane in anisotropic plasma. Optik 2020;224:165677. https://doi.org/10.1016/j.ijleo.2020.165677.

[43] Liu X, Shu M, Chen X, Zhang A. Four-dimensional characteristic matrix for electromagnetic coupling of multilayer sub-wavelength metasurface system. IEEE Trans Electromagn Compat 2020;62(6):2765–72.

[44] Xu Q, Liu X, Xuan Y, Xu Y, Liu D. High-performance infrared thermal radiation suppression metamaterials enabling inhibited infrared emittance and decreased temperature simultaneously. Int J Heat Mass Transf 2020;161:120318. https://doi.org/10.1016/j.ijheatmasstransfer.2020.120318.

[45] Jia P-Z, Wu D, Zhang Q-Q, Zhou W-X, Fan Z-Q, Feng Y-X, et al. Design of thermal metamaterials with excellent thermal control functions by using functional nanoporous graphene. Phys Status Solidi-Rapid Res Lett 2020;14(10):2000333. https://doi.org/10.1002/pssr.v14.1010.1002/pssr.202000333.

[46] Wu F, Huang W, Chen W-Y, Xiao Y, Yu D-L, Wen J-H. Design of subwavelength broadband hybrid sound absorption structure based on micro-perforated plate and coiled channels. Acta Phys 2020;69(13).

[47] Long H, Liu C, Shao C, Cheng Y, Chen K, Qiu X, et al. Subwavelength broadband sound absorber based on a composite metasurface. Sci Rep 2020;10(1). https://doi.org/10.1038/s41598-020-70714-7.

[48] Amer AAG, Sapuan SZ, Nasimuddin, Binti Zinal N. Metasurface with wide-angle reception for electromagnetic energy harvesting. In: Proceedings of the 11th National Technical Seminar on Unmanned System Technology 2019. NUSYS'19. Lecture Notes in Electrical Engineering, ed. Z. Md Zain, et al. 2021, p. 693–700.

[49] Wang J, Dai G, Huang J. Thermal metamaterial: fundamental, application, and outlook. Iscience 2020;23(10).

[50] Liu Y, Li Y-F, Liu X-Z. Manipulation of acoustic wavefront by transmissive metasurface based on pentamode metamaterials. Chin Phys B 2019;28(2):024301. https://doi.org/10.1088/1674-1056/28/2/024301.

[51] Tang L, Yang Y. Analysis of synchronized charge extraction for piezoelectric energy harvesting. Smart Mater Struct 2011;20(8):085022. https://doi.org/10.1088/0964-1726/20/8/085022.

[52] Bhatnagar PL, Gross EP, Krook M. A model for collision processes in gases. I. Small amplitude processes in charged and neutral one-component systems. Phys Rev 1954;94(3):511–25.

[53] Suga K, Kuwata Y, Takashima K, Chikasue R. A D3Q27 multiple-relaxation-time lattice Boltzmann method for turbulent flows. Comput Math Appl 2015;69(6):518–29.

[54] Han S, Yu R, Li Z, Wang Y. Effect of turbulence model on simulation of vehicle aerodynamic characteristics based on XFlow. In: Frontiers of Mechanical Engineering and Materials Engineering Ii, Pts 1 and 2, W.P. Sung, J.C.M. Kao, and R. Chen, Editors. 2014. p. 1571–1574.

[55] Barrero-Gil A, Alonso G, Sanz-Andres A. Energy harvesting from transverse galloping. J Sound Vib 2010;329(14):2873–83.

[56] Ng YT, Luo SC, Chew YT. On using high-order polynomial curve fits in the quasi-steady theory for square-cylinder galloping. J Fluids Struct 2005;20(1):141–6.

[57] Abdelkefi A, Hajj MR, Nayfeh AH. Power harvesting from transverse galloping of square cylinder. Nonlinear Dyn 2012;70(2):1355–63.

[58] Zhu H, Tang T, Zhou T, Liu H, Zhong J. Flow structures around trapezoidal cylinders and their hydrodynamic characteristics: effects of the base length ratio and attack angle. Phys Fluids 2020;32(10):103606. https://doi.org/10.1063/5.0021043.

[59] Zou QF, Ding L, Wang HB, Wang JL, Zhang L. Two-degree-of-freedom flow-induced vibration of a rotating circular cylinder. Ocean Eng 2019;191:11.